Prevention of tissue damage by water jet during cavitation

Daniel Palanker,[a] Alexander Vankov, and Jason Miller
Department of Ophthalmology, School of Medicine and W. W. Hansen Experimental Physics Laboratory, Stanford University, Stanford, California 94305

Menahem Friedman and Moshe Strauss
Nuclear Research Center, Negev, P.O. Box 9001, Beer Sheva, Israel

(Received 16 September 2002; accepted 2 June 2003)

Cavitation bubbles accompany explosive vaporization of water following pulsed energy deposition in liquid media. Bubbles collapsing at the tip of a surgical endoprobe produce a powerful and damaging water jet propagating forward in the axial direction of the probe. We studied interaction of such jet with tissue using fast flash photography and modeled the flow dynamics using a two-dimensional Rayleigh-type hydrodynamic simulation. Maximal velocity of the jet generated at pulse energies of up to 1 mJ was about 80 m/s. The jet can produce tissue damage at a distance exceeding the radius of the cavitation bubble by a factor of 4. We demonstrate that formation of this flow and associated tissue damage can be prevented by application of the concave endoprobes that slow down the propagation of the back boundary of the bubble. Similar effect can be achieved by positioning an obstacle to the flow, such as a ring behind the tip. © *2003 American Institute of Physics.* [DOI: 10.1063/1.1593803]

I. INTRODUCTION

Pulsed lasers and electric discharges delivered into the eye via optical fibers or microelectrodes are capable of precise dissection of soft tissue in liquid media. Such techniques have been applied to intraocular surgery in both anterior and posterior poles.[1–5] The mechanism of interaction in most of these applications involves pulsed energy deposition under heat confinement conditions, i.e., pulse duration is short enough to prevent heat diffusion away from the energy deposition zone. (Pulses of less than 1 μs in duration are required to limit the heat diffusion to a distance under 1 μs). Overheated water (whether by direct absorption of the pulse energy[2,4,5] or by heat transfer from the light-absorbing tissue matrix[3,6]) undergoes explosive vaporization creating a rapidly expanding vapor cavity.[7] The shock wave and shear stress associated with expansion of this cavity may result in the fragmentation of the tissue in its proximity. During collapse of the cavity (cavitation bubble), a fast water jet may form causing severe damage to tissue far away from the initial energy deposition site. This secondary damage mechanism has been a major factor limiting the precision, safety, and thus applicability of the pulsed endosurgical techniques to microsurgery.[8]

In this article, we study the mechanisms of jet formation during collapse of the cavitation bubble on the endoprobe and propose a technique for preventing jet formation. We quantify the extent of collateral damage introduced by a pulsed electrosurgical device, called PEAK (pulsed electron avalanche knife), on a model tissue—the chick choriallantoic membrane. Specifically, we measure the width of the induced damage zone and the maximum distance between probe and tissue at which tissue is damaged as a function of pulse energy for various probe geometries. Since water jet is produced during the collapse of a bubble only in the presence of an obstacle (e.g., such as a tissue surface or an endoprobe), we hypothesize that the flow might be reduced by altering the shape of the probe. We demonstrate that the water jet can indeed be reduced, and even completely eliminated by optimizing the shape of the endoprobe. This effect leads to substantial improvement in precision and safety of the pulsed endosurgery.

Finally, in order to find a simple engineering solution for eliminating the water jet, we numerically simulate the cavitation bubble dynamics using a two-dimensional Rayleigh type hydrodynamic code by applying finite element methods. We determine the minimal size of a ring-shaped obstacle positioned behind the tip of the probe needed for prevention of the formation of the water jet.

II. MATERIALS AND METHODS

A. Experimental methods

In this study cavitation bubbles are created using the pulsed electron avalanche knife (PEAK)—a device for dissection of soft tissue in liquid media by plasma-mediated electric discharges.[4] PEAK was operated with 100 ns-long high voltage (several kV) pulses applied to a 25 μm wire embedded in a tapered insulator with various tip shapes. The end of the wire was exposed to a conductive liquid medium (typically saline) while a concentric stainless steel needle of 0.9 mm in diameter (20 G) served as the return electrode.

Dimensions of the cavitation bubbles were measured using fast flash (about 0.5 μs) shadow photography with a fast light emitting diode (LMR51WF, Sunled Corp., Walnut Creek, California). For these measurements the probe was immersed into an isotonic saline solution in a Petri dish positioned on an inverted microscope (IMT-2, Olympus), and

[a]Electronic mail: palanker@stanford.edu

 © 2003 American Institute of Physics

Downloaded 12 Sep 2003 to 171.64.108.234. Redistribution subject to AIP license or copyright, see http://ojps.aip.org/japo/japcr.jsp

the image was captured using a charge coupled device (CCD) camera (NL/CCD-512, Princeton Instruments, Trenton, NJ). For measurement of flow velocity during the poorly reproducible phases of bubble collapse, a double-flash was applied with 1.5 μs delay between the flashes. The images produced by both flashes were recorded on the same frame of the CCD.

As a model of soft tissue, we used the chorioallantoic membrane (CAM) from white leghorn chicken embryos 14–18 days into incubation. The zone of collateral damage was assessed using propidium iodide (PI), which has been shown to be a sensitive fluorescent indicator of cell permeability.[9,10] In those cells with loss of membrane integrity, whether that loss is temporary or permanent, PI can enter and bind to its preferred target, nucleic acids.[9,10] A piece of CAM was excised and pinned down to a Petri dish lined with 0.8% agarose. The sample was then covered with a saline solution containing PI at a concentration of 4 μM and loaded onto a fluorescent inverted microscope. The PEAK probe was positioned at a 45° angle to the tissue surface using an XYZ micromanipulator. One pulse and 50 pulses (at repetition rate of 5 Hz) were applied at various distances from the tissue. The size of the fluorescent zone was measured using a CCD camera (NL/CCD-512, Princeton Instruments) with WinView-32 software. Reproducibility of the damage zones created by PEAK was confirmed by repeating the experiments three times.

B. Numerical simulations

Computation of the evolution of a vapor bubble in water requires two-dimensional (2D) hydrodynamic simulations and therefore sophisticated computational capabilities.[11] Recently a 2D Rayleigh-type model has been developed that can be applied for an incompressible flow induced by a cylindrically symmetric probe.[12]

Since the fluid outside the bubble is incompressible and irrotational to a good approximation throughout most of the bubble expansion and collapse,[13] our model is based on introducing a flow potential ϕ which is a solution to Laplace's equation[14] and determines the fluid velocity outside the bubble by $\mathbf{u}=-\nabla\phi$. This approach was previously applied for treating cavities using finite differences and boundary integral methods.[15,16]

In this work we use a general finite element code which was designed to solve elliptic partial differential equations over a bounded domain with moving boundaries. As in the Rayleigh model we assume that the inside of the bubble is uniform in pressure and density and derive a moving boundary condition for ϕ at the bubble boundary. For every time step an unstructured mesh finite element solver[12,17] is applied to update the triangulation outside the bubble.

Integrating the hydrodynamic equations of continuity for the density ρ and momentum for the velocity $\mathbf{u}$ and assuming a constant ρ, we obtain,[12]

$$\frac{d\Phi(\theta)}{dt}=\frac{p-p_\infty}{\rho}-\frac{U^2(\theta)}{2}, \tag{1}$$

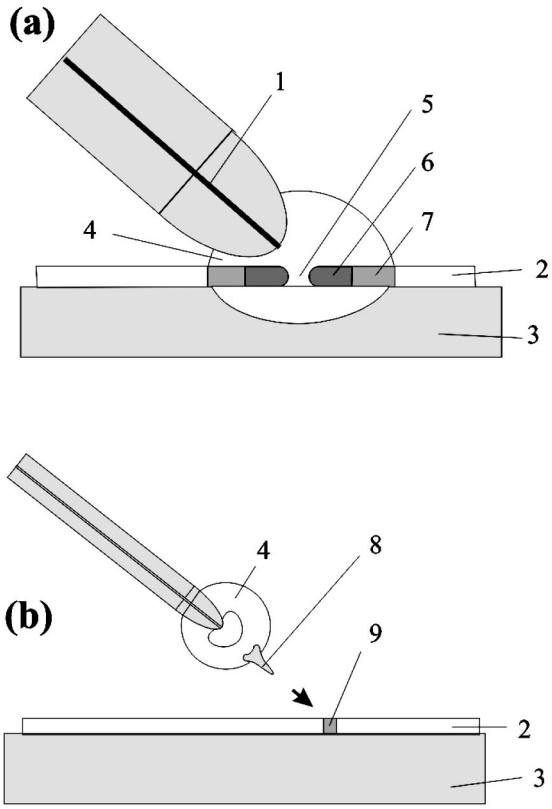

FIG. 1. Diagram of the interaction between the cavitation bubble and tissue. 1: a 25 μm wire electrode embedded into glass insulator. 2: a thin tissue sample (CAM) is pinned on top of a transparent gel (3). The probe and the sample are immersed into a physiological medium (isotonic saline solution) bathed with a propidium iodide solution. The Petri dish with sample is mounted on an inverted fluorescent microscope equipped with fast LED for fast shadow photography. 4: is a transient (cavitation) bubble; 5: a crater, 6: a confluent staining zone, and 7: speckled zone. (a) The endoprobe is positioned in contact with tissue. (b) The probe is positioned away from tissue and oriented at 45° to its surface. The point of interaction between the water jet (8) and tissue (9) is a tissue damage area.

where Φ and $\mathbf{U}$ are the flow potential and the velocity at the bubble boundary, p and $p_\infty=1\,at$ are the bubble pressure and the ambient pressure, respectively, ρ is the outer fluid density, and θ parametrizes the distance along the bubble boundary. The basis for our 2D time dependent model is solving the Laplace equation for ϕ applying the moving boundary condition [Eq. (1)] and the adiabatic nature of the process for updating the bubble's physical parameters.[12] This model assumes incompressible flow of fluid with zero viscosity. In the final stage of the bubble collapse compressible effects such as acoustic emission and viscosity cause dissipation of the bubble energy.

III. RESULTS AND DISCUSSION

A. Radius of the damage zone

In the first set of experiments we measured the size of the damage zone produced by the PEAK probe applied in contact with the tissue [see Fig. 1(a)]. The damaged area can typically be divided into three distinct zones. The first, centrally located zone has low fluorescence and corresponds to a crater in tissue. The second (paracentral) zone stains with a dense, confluent fluorescence. Since PI stains primarily

Downloaded 12 Sep 2003 to 171.64.108.234. Redistribution subject to AIP license or copyright, see http://ojps.aip.org/japo/japcr.jsp

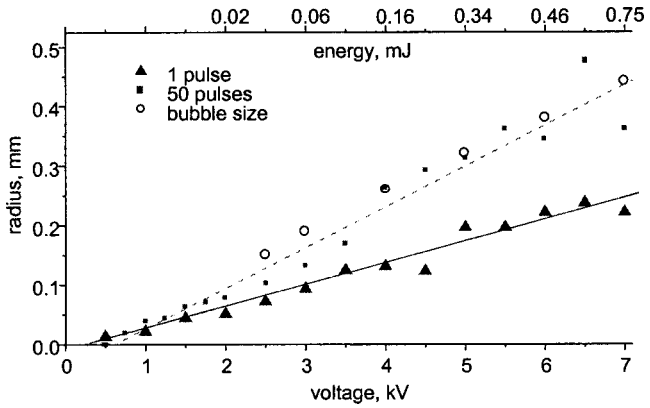

FIG. 2. Radius of the speckled damage zone in tissue produced by 1 and by 50 pulses, as compared to the maximal radius of the cavitation bubble at various voltages.

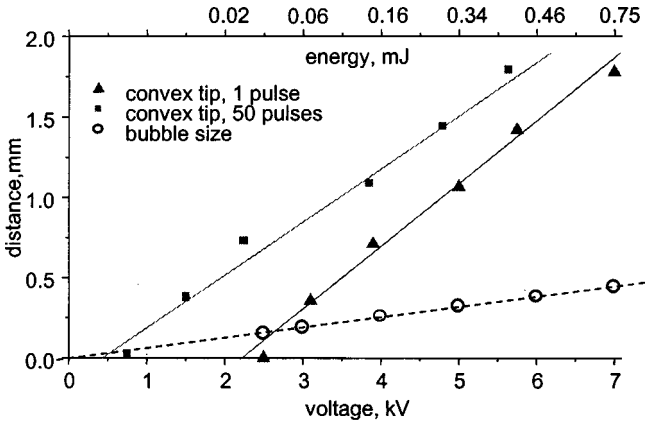

FIG. 3. "Minimal safe distance" between the *convex* probe and tissue at which no damage is induced by application of 1 and 50 pulses as a function of the voltage (lower scale) or pulse energy (upper scale).

nucleic acids,[9,10] a zone of confluence suggests that nuclear material in this area has been scattered across the entire cell. Thus, the confluent zone most likely represents a set of cells that have been structurally disrupted by PEAK. The third peripheral zone stains in a speckled, much less dense pattern. This speckled appearance suggests that only the nuclei of some cells in this region have been stained with PI (and that these stained cells are structurally intact, with nuclear material clearly separated from the rest of the cell) while other cells in the speckled region do not stain with PI at all.

Application of a single pulse of PEAK in contact with tissue at voltages varying between 0.5 and 7 kV (corresponding pulse energies varying between 1 μJ and 0.75 mJ) resulted in the damage zones with radii ranging from 0 to 110 μm for the confluent zone, and from 13 to 220 μm for the speckled zone. For comparison, cutting of the detached retina is performed at 3–4 kV (corresponding to pulse energies of 64–150 μJ).[4,18] The largest zone of damage, i.e., the speckled zone is plotted in Fig. 2. Applications of 50 pulses (when the size of the collateral damage zone in tissue reaches saturation) produced a damage zone with a radius ranging from 0 to 225 μm for the confluent zone and from 37 to 415 μm for the speckled zone (see the speckled zone size on Fig. 2). The size of the maximal damage zone (speckled zone after application of 50 pulses) is practically identical to the maximal size of the cavitation bubble at each respective voltage.

B. Minimal safe distance

Tissue damage may be produced not only by an impingement of an expanding cavitation bubble into tissue, but also by a water flow induced by collapsing bubble in front of the probe. This jet may propagate and impinge on tissue several millimeters away from the probe, similar to the jet forming during collapse of the dielectric breakdown-induced bubbles in a proximity of tissue surface.[19] To evaluate the influence of such water flow on soft tissue we measured the minimal distances between the probe and tissue at which fluorescence was introduced at various pulse energies [see Fig. 1(b)]; we dubbed this distance the "minimal safe distance." Results obtained with 1 and 50 pulses applied to the convex probe with a 200 μm tip diameter are shown in Fig. 3. Very similar results were obtained with the convex probe of a 100 μm tip diameter (not shown in this graph). For one pulse the minimal safe distance at the voltage range applicable to vitreoretinal surgery (2 to 4 kV corresponding to pulse energies ranging from 0.017 to 0.15 mJ) varies from 0.05 to 0.8 mm, while for 50 pulses it reaches 1.1 mm. These distances are substantially (by a factor of 4) larger than the maximal size of the cavitation bubble at respective voltage indicating on the fact that the tissue damage in this case was introduced by the water flow rather than by the direct contact with the bubble. Another indication on this effect was the fact that the spot of damage was found always along the axis of the probe (positioned at 45° to the tissue), and not directly under the probe, where the distance between the tip and the tissue would be the shortest.

C. Dynamics of cavitation

The dynamics of the cavitation bubble growing and collapsing on the endoprobe after application of the 0.15 mJ pulse is shown in the sequence of photographs in Fig. 4. Delay (in μs) between the 100 ns long electric discharge and 500 ns long light-emitting diode flash is shown in the right lower corner of each frame. The bubble collapses asymmetrically moving forward from the tip and reaches its minimal size at 56 μs. It then regrows and collapses several times until it completely disappears at about 200 μs after the pulse.

Since the bubble is practically empty during the phase of maximal expansion, its potential energy can be estimated as $E=PV$, where P is the ambient pressure, and V is the volume of the bubble. In our case the energy of the bubble was found to be proportional to the pulse energy with a coefficient of 0.05 (i.e., 5% of the discharge energy is converted into mechanical energy of the cavity).

Velocity of the bubble boundaries can in principle be measured by acquiring two pictures at different delay times measured in two separate discharges. The lifetime of the bubble is proportional to the maximal radius of the bubble, and thus it varies with the pulse energy. Since the pulse–to–pulse variation of the discharge energy was on the order of

Downloaded 12 Sep 2003 to 171.64.108.234. Redistribution subject to AIP license or copyright, see http://ojps.aip.org/japo/japcr.jsp

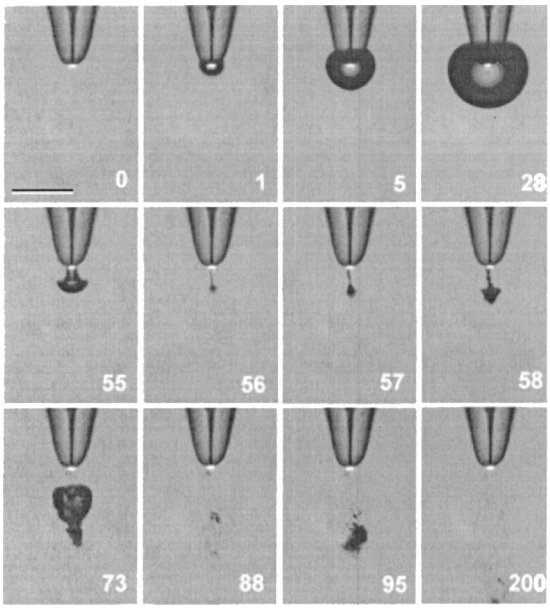

FIG. 4. Dynamics of PEAK cavitation bubble growth and collapse in front of the endoprobe after application of a 100 ns long, 0.15 mJ pulse. Delay (in μs) between the pulse and a 0.5 μs long flash is shown in the corner of each frame. Scale bar shown on the first frame is 0.5 mm.

2%, the corresponding collapse jitter was on the order of 1 μs. Such a substantial variation in timing of the collapse makes the measurements of the boundary displacement in two separate events quite unreliable. To overcome this difficulty we applied a series of two flashes (0.5 μs duration separated by 1.5 μs) for each photograph. In this approach the two boundaries can be clearly observed (see for example Fig. 5), and thus the boundary velocity can be reliably calculated. We measured axial component of the flow velocity at the back (upper) and front (lower) boundaries of the collapsing cavity, and the results are plotted in Fig. 6. Since velocity of the back boundary is substantially higher than the velocity of the front part of the bubble, the water jet forming during the collapse of the bubble propagates in the forward direction. The application of repetitive pulses results in the formation of a stationary flow easily observable by surgeon and indicating on direction of the jet.

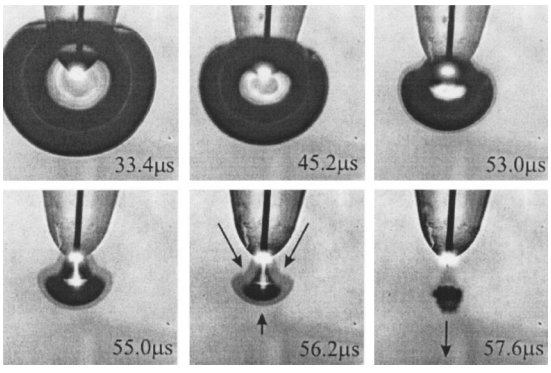

FIG. 5. Collapsing bubble on a convex tip photographed with two 0.5 μs-long pulses of LED separated by 1.5 μs. Delay between the beginning of the discharge and beginning of the flash is shown in the corner of each frame.

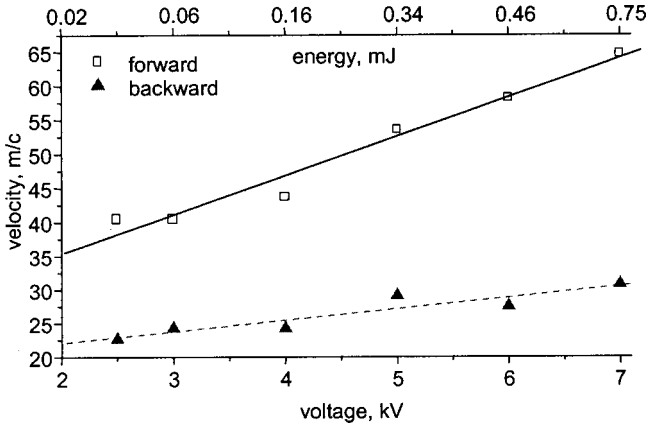

FIG. 6. Vertical component of the bubble boundary velocity measured 1 μs before collapse on a convex probe. Back side of the bubble propagates forward about 2.5 times faster than the front side propagates backward.

D. Effect of the probe geometry on jet formation

Asymmetry in the collapse of the bubble is introduced by the presence of the nearby boundaries, such as the surface of tissue[20] or a probe.[21] In the case of a symmetric collapse of a spherical bubble, the flow is radial, and thus the bubble would probably be undisturbed if the probe would have a conical shape with its apex located in the center of the bubble. (In this statement we neglect possible effects of the surface tension and friction at the interface of the bubble with the probe). However, in practice the surgical probes are never ideally conical: to avoid piercing of the soft tissue by

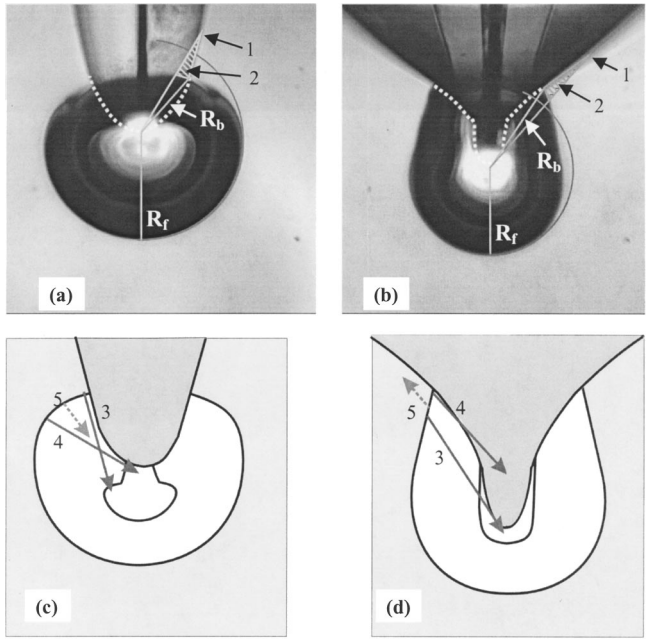

FIG. 7. The back boundary (radius R_b) of the bubble collapsing on a convex probe [frames (a) and (c)] is accelerated due to the fact that the flow is converging faster than in the spherical front part of the bubble (radius R_f), since part of the liquid volume (2) is replaced by the probe. Position of the bubble at maximal expansion phase is indicated by number 1. Relative acceleration of the back boundary is shown in frame C by the arrow 5. On the concave probe [frames (b) and (d)], the relative cross-section of the flow increases as the bubble collapses and thus the boundary is decelerated (5), as compared to the spherical front part of the bubble.

Downloaded 12 Sep 2003 to 171.64.108.234. Redistribution subject to AIP license or copyright, see http://ojps.aip.org/japo/japcr.jsp

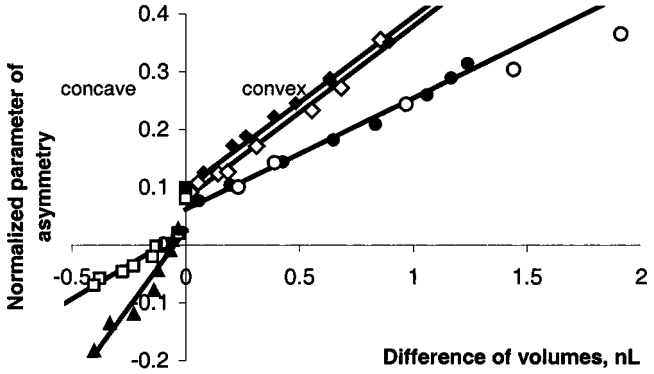

FIG. 8. Normalized parameter of asymmetry of the collapsing bubble with three convex and two concave tips vs parameter of difference of volumes $V(R)=V_{\text{real}}-V_{\text{conical}}$. Discharge energy is 0.15 mJ. Maximal difference of volumes is used as the parameter best representing tip shape. Convex probes (to the right of the Y axis): ◇: 1.5 nL, ■: 2.7 nL; ●: 3.1 nL; and ○: 4.3 nL. Concave probes (to the left of the Y axis): □: −1.5 nL, and ▲: −2.5 nL.

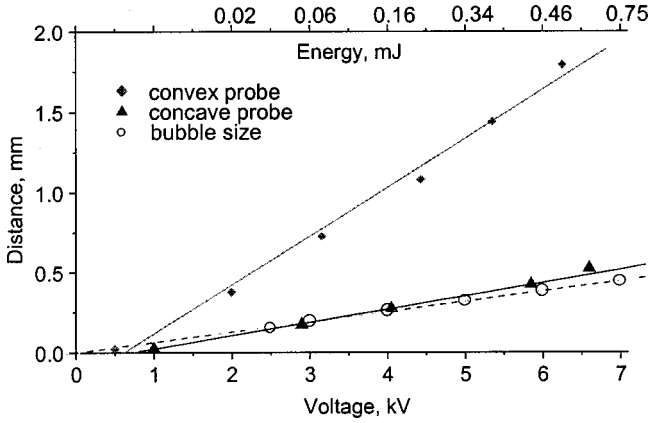

FIG. 10. Comparison of the minimal safe distances (MSD) between the probe and tissue measured with a convex and a concave probe (50 pulses) at various discharge voltages. MSD for the concave probe practically coincides with maximal bubble radius and is much (~4×) smaller than the MSD of the convex probe at each corresponding voltage.

mere contact with the probe the radius of curvature at the tip must be at least 50 μm, thus making the probe convex. This convexity ensures that a part of the volume that would be available for an unhampered water flow with the conical tip is instead occupied by the probe [see Figs. 7(a) and 7(c)]. Thus, according to the Bernoulli equation, flow is accelerated with decreasing cross-sectional area.

Assuming that distortion of the bubble from its spherical shape is determined by the deviation of the probe geometry from an ideal cone, we plot in Fig. 8 a normalized factor of asymmetry of the bubble $E=(R_{\text{forw}}-R_{\text{back}})/(R_{\text{forw}}+R_{\text{back}})$ as a function of a cumulative difference in volumes between the conical and the experimental tips, as shown in Figs. 7(a) and 7(b). Each series in the plot on Fig. 8 represents a history of the collapse of a bubble on one type of the probe. Discharge energy of 0.15 mJ was applied in each of these experiments. Zero volume corresponds to the beginning of the collapse (i.e., maximal expansion of the bubble), and maximal volume corresponds to the end of the collapse. Three different types of the convex probes are presented on the right side of the graph: a cylindrical probe with a flat end of 120 μm in diameter and two tapered probes—one with a flat and the other with a rounded end of 200 μm in diameter (shown in the left frame of Fig. 7). Nonzero initial asymmetry of the bubble (at zero volume) represents the fact that even at maximal expansion the bubble is not perfectly spherical—its back side (adjacent to the probe) is a little shorter due to the interference of the probe during expansion. As one can see in Fig. 8, during collapse an asymmetry of the bubble significantly increases.

Water jet velocity should theoretically be inverted by the application of a concave probe, where cross-sectional area available for fluid flow increases at the back of the bubble as the bubble collapses, resulting in deceleration of the bubble's back side, as shown in Figs. 7(b) and 7(d). To test this idea, we created a concave endoprobe expanding the upper part of a thin glass electrode by adding a droplet of glue above the tip. As can be seen in Figs. 7–9, the dynamics of bubble collapse with these concave probes did indeed change; the bubble collapsed towards the probe, and no forward-propagating jet formed. Note in Fig. 8 that initial (maximal expansion phase) asymmetry for both the convex and the

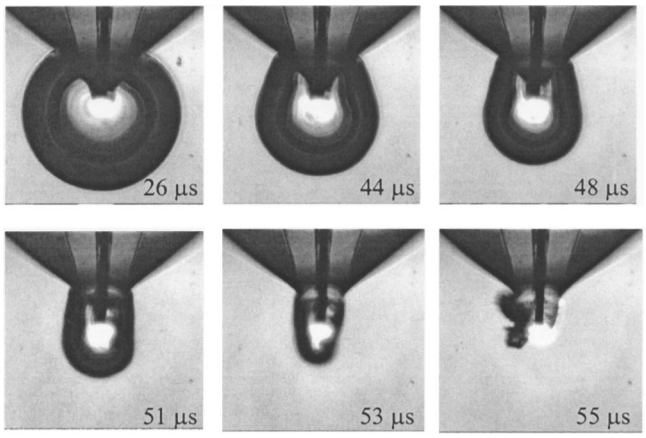

FIG. 9. Dynamics of bubble collapse on a concave probe. Delay between the pulse and the flash is shown in the corner of each frame. Note that bubble boundary reaches the surface of the probe almost simultaneously in every part of the boundary and thus no water jet is created.

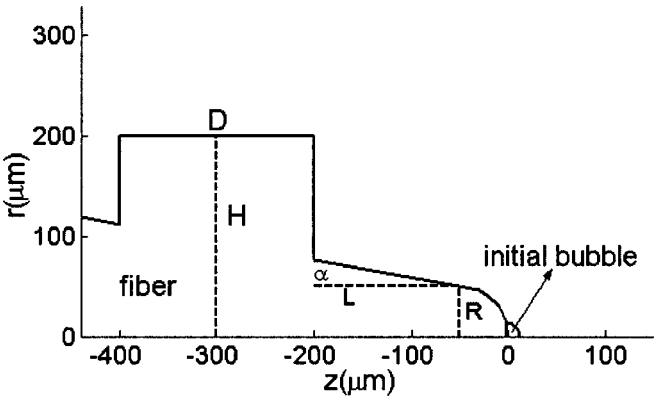

FIG. 11. Schematics of a cylindrically symmetric conical fiber with a spherical tip and a ring shaped obstacle: $R=50$ μm; $L=150$ μm; $D=200$ μm; and $\alpha=10°$. The probe tip orientation has been rotated 90° counterclockwise from all previous figures.

Downloaded 12 Sep 2003 to 171.64.108.234. Redistribution subject to AIP license or copyright, see http://ojps.aip.org/japo/japcr.jsp

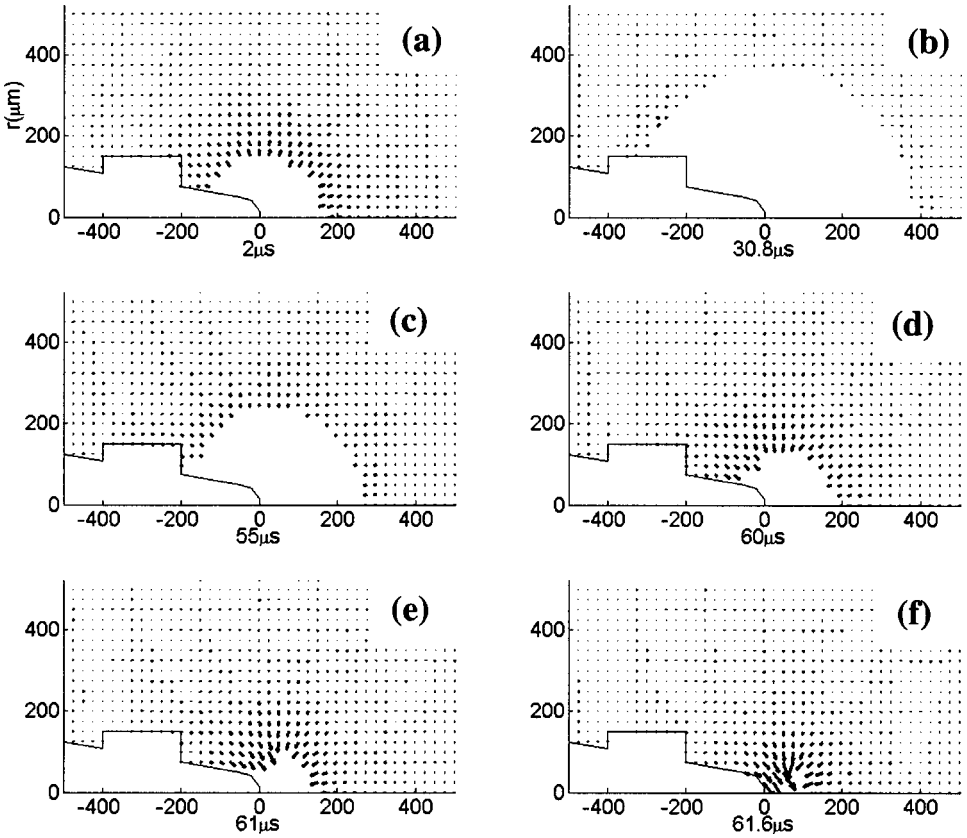

FIG. 12. Map of fluid velocity during expansion and collapse of the bubble in cylindrical coordinates r,z at various times after energy deposition: 2, 30.8 (maximum expansion), 60.4, and 61 μs (frames a–f, respectively). With a ring of radius 150 and width of 200 μm, a rightward (forward-propagating) jet is created.

concave probes has the same (positive) sign, indicating on the fact that back radius of the bubble is shorter than the front one. Smaller radius of curvature of the bubble leads to higher initial acceleration of the back boundary for both types of the probe.[20] This asymmetry is stronger for the convex than for the concave probe thus leading to faster acceleration of the back boundary in the case of the convex probe. However, during collapse on the concave probe this asymmetry parameter inverts, meaning that due to the effect of the probe the bubble's back boundary eventually decelerates as compared to its front.

Measurements of the minimal safe distance with concave tips (results are plotted in Fig. 10) proved that prevention of the jet formation eliminates the tissue damage associated with it, and thus reduces the axial range of damage to the size of the bubble itself. In addition, the point of damage in this case was found always under the tip, and not in front of it, which also indicates that the damage is introduced by the expanding spherical bubble, and not by the water jet, as it was with the convex probes. As can be seen in Fig. 10, with the application of concave probes the range of tissue damage is reduced by a factor of 4, thus making the pulsed laser and electrical endoprobes much safer and more precise instruments.

E. Simple solution: An obstacle behind the tip

To prevent mechanical damage to tissue by a sharp tip typical surgical probe has a flat or rounded end, which makes it convex. To compensate for that, a concave area can be added above the tip. In this case the actual flow dynamics will depend on the ratio of the concave and convex parts, i.e., it will change with the size of the bubble and thus with the pulse energy. One way to evaluate whether a jet will form during bubble collapse at a particular pulse energy is to observe the bubble dynamics using fast shadow photography. However, this technique requires some special equipment and skills. A significantly easier observable indicator for generation of a water jet is a stationary flow that forms during repetitive pulse application. Such flow can be readily observed in water especially if it contains visible particles or small bubbles. At low pulse energies, when the transient bubble does not reach the concave part of the probe, forward-directed flow occurs. At higher energies the flow is stopped, and then reversed, due to the overwhelming influence of the concave part of the probe.

A simple way of manufacturing the concave tips would be to position an obstacle, such as a flat ring behind the tip at the distance not exceeding the maximal radius of the bubble. Such a ring has exactly the same effect as a concave probe and can prevent formation of the forward-propagating water jet. The effect of such an obstacle is similar to the effect of a boundary impeding flow of liquid towards the collapsing bubble. Such a restriction leads to the formation of a jet towards this boundary.[20] This ring can be made of a heat-shrink polymer, for example. To minimize interference with tissue manipulation and observation during surgery it should be made as small as possible. To calculate the minimal size of the disk sufficient for prevention of jet formation, we used the numerical simulations.

Downloaded 12 Sep 2003 to 171.64.108.234. Redistribution subject to AIP license or copyright, see http://ojps.aip.org/japo/japcr.jsp

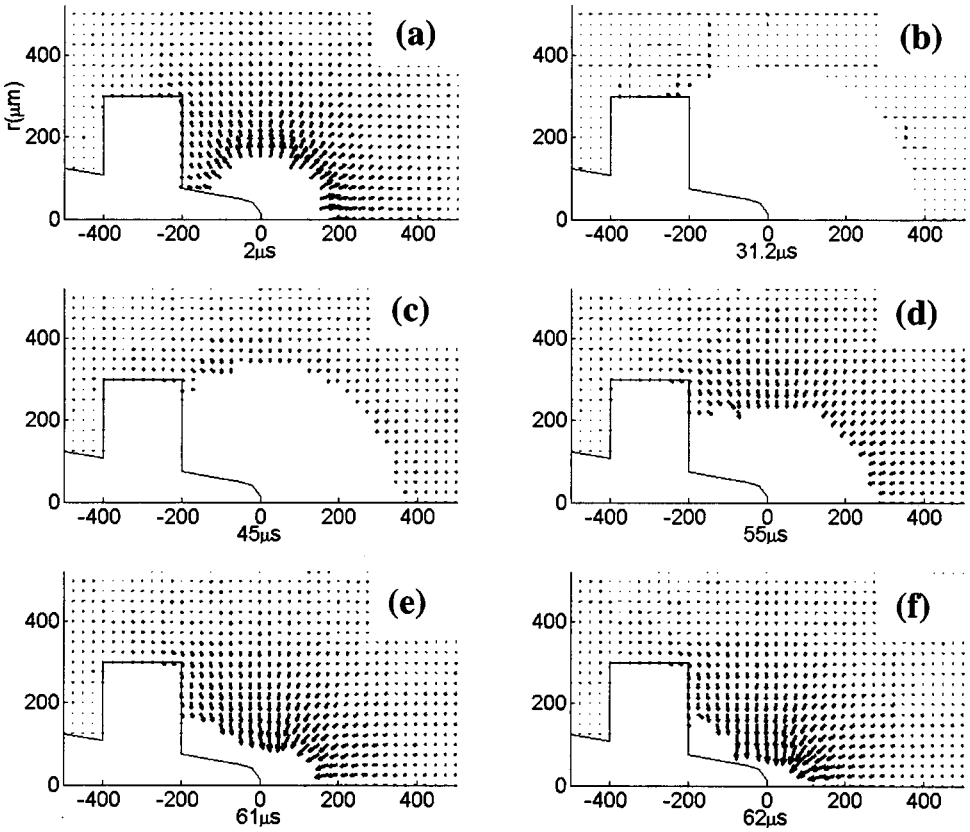

FIG. 13. Map of fluid velocity during expansion and collapse of the bubble in cylindrical coordinates r,z at various times after energy deposition: 2, 31.3 (maximal expansion), 61.8, and 62.3 μs (frames a–f, respectively). With a ring of 300 μm in radius and 200 μm in width, a rightward jet is *not* created, and the collapse of the bubble occurs towards the probe.

F. Results of numerical simulations

Throughout the simulation we considered a cylindrically symmetric conical probe, with a slope of 10°, and with a ring as presented in Fig. 11. The probe ends with a semispherical tip of radius $R=50$ μm. The ring-shaped obstacle, normal to the probe's axis of symmetry, is positioned at the distance of 200 μm from the probe's tip. The radius and the width of the ring are noted by parameters H and D, respectively. The initial bubble parameters were chosen as follows: (1) assuming that the hemispherical volume occupied by plasma at the end of the discharge is fully vaporized, the mass of the vapor can be estimated by measuring the size of the ionized zone. At a discharge energy of 0.15 mJ this radius was 15 μm, corresponding to the vapor mass of 7 ng; (2) bubble produced on a flat boundary 0.7 μs after the discharge of the same energy had a radius of 90 μm and a boundary velocity of 45 m/s. To match the observables (1) and (2) the following initial conditions of the model bubble have been chosen: Assuming isochoric heating during the discharge, initial density was taken to be $\rho=1$ g/cm^3, boundary velocity 410 m/s, and entropy $S=3.4\text{J}/(\text{g K})$. By using the (NBS) Steam Tables[22] we obtained a bubble initial pressure of $p=8350$ bar and temperature of $T=468\,^{\circ}\text{C}$. The energy inside the bubble and in the moving liquid is 0.013 mJ. The bubble evolves adiabatically with a relation between the internal physical parameters according to the NBS tables with a constant entropy.

The bubble expands around the spherical tip, propagates towards the ring, and then turns back. Since we limited ourselves to bubbles that do not expand beyond the ring's left side, we assumed the width of the ring to be 200 μm, which was sufficient for all heights (ring radii) considered. The expansion and collapse of the bubble is shown in Fig. 12 for a ring of radius 150 μm, and in Fig. 13 for a ring of radius 300 μm. Each figure consists of four stages: (a) early stage of expansion, (b) maximum bubble, and (c–d) final stages of collapse.

Determination of whether a jet is created or not has been conducted as follows. During the collapse stage we need to consider two collapse velocities. The first, v_R is the velocity of the right edge of the bubble towards the probe ($v_R<0$). The second, v_j is the maximum velocity of the left side of the bubble boundary, provided that only points to the right of the probe's tip with positive horizontal velocity are considered. Thus $v_j>0$ and it measures creation of a rightward jet. Thus, v_j+v_R is an effective jet formation velocity. If it is positive at the final stage of the collapse, a forward-propogating jet is created. If $v_j+v_R<0$ the bubble collapses on the probe. The value of v_j+v_R is measured at the moment when the bubble's right edge is about 100 μm from the probe tip; empirically we have determined that the direction of water jet flow is visually clear at this distance.

The most important result is that a large ring prevents creation of a rightward jet at the final stage of the collapse (Fig. 13) while a small ring does not stop the jet (Fig. 12). Fig. 14 plots v_j+v_R versus the ring's radius; the graph indicates that the turning point for the water jet occurs somewhere between a radius of 250 and 300 μm. This result suggests that for applications involving caviation bubbles larger than 0.6 mm (corresponding to the pulse energy of above 0.1 mJ) a ring of about 0.6 mm in diameter positioned 0.2 mm behind the tip will prevent formation of the water jet.

Downloaded 12 Sep 2003 to 171.64.108.234. Redistribution subject to AIP license or copyright, see http://ojps.aip.org/japo/japcr.jsp

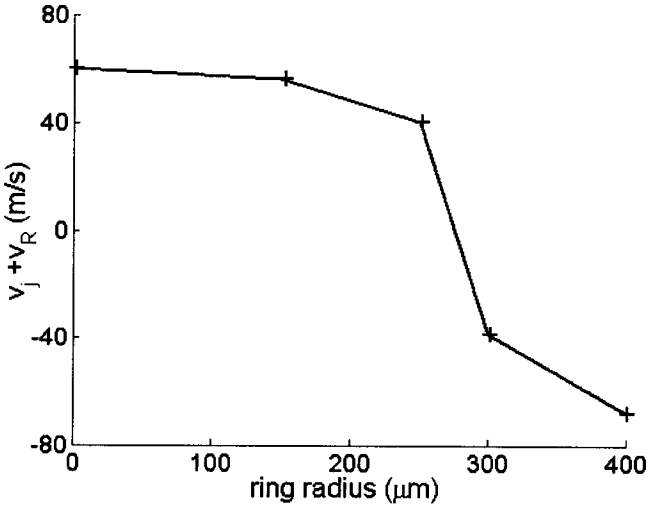

FIG. 14. Effective fluid velocity ($v_j + v_R$) vs radius of the ring obtained in numerical simulations. Note that jet velocity changes signs somewhere between a ring radius of 250 and 300 μm.

IV. CONCLUSIONS

We have demonstrated that in pulsed endosurgery, when pulse duration is in a microsecond or submicrosecond domain, the tissue damage is dominated by effects of cavitation bubbles. When the endoprobe is in contact with tissue the maximal size of the damage zone is equal to size of the cavitation bubble at maximal expansion. When the probe is held at some distance from the tissue a powerful jet can form during cavitation, and it damages tissue at distances up to four times larger than radius of the bubble. Such jet is a major factor limiting precision and safety in pulsed endosurgery. Jet formation can be prevented if a concave, rather than a convex endoprobe is applied. Alternatively, a ring-shaped obstacle can be positioned behind the tip thus preventing the formation of the jet. Either option allows for significant reduction in consequent tissue damage and improvement in the precision and safety of pulsed endosurgical instrumentation.

ACKNOWLEDGMENTS

This work was funded in part by the National Institutes of Health (National Eye Institute, grant # RO1 EY12888-01A1) and by Carl Zeiss Inc.

[1] D. J. D'Amico, P. D. Brazitikos, G. R. Marcellino, S. M. Finn, and J. L. Hobart, Am. J. Ophthalmol. **121**(4), 414 (1996).
[2] C. P. Lin, D. Stern, and C. A. Puliafito, Invest. Ophthalmol. Visual Sci. **31**(12), 2546 (1990).
[3] D. Palanker, I. Hemo, I. Turovets, H. Zauberman, G. Fish, and A. Lewis, Invest. Ophthalmol. Visual Sci. **35**(11), 3835 (1994).
[4] D. V. Palanker, J. M. Miller, M. F. Marmor, S. R. Sanislo, P. Huie, and M. S. Blumenkranz, Invest. Ophthalmol. Visual Sci. **42**(11), 2673 (2001).
[5] D. Palanker, I. Turovets, and A. Lewis, J. Appl. Phys. **81**(11), 7673 (1997).
[6] D. Palanker, I. Turovets, and A. Lewis, Lasers Surg. Med. **21**(3), 294 (1997).
[7] I. Turovets, D. Palanker, and A. Lewis, Photochem. Photobiol. **60**(5), 412 (1994).
[8] J. M. Miller, D. V. Palanker, A. Vankov, M. F. Marmor, and M. S. Blumenkranz, Arch. Ophthalmol. Rev. Gen. Ophthalmol. **121**, 871 (2003).
[9] D. J. Arndt-Jovin and T. M. Jovin, Methods Cell Biol. **30**, 417 (1989).
[10] M. J. Waring, J. Mol. Biol. **13**(1), 269 (1965).
[11] R. A. London, M. E. Glinsky, G. B. Zimmerman, D. S. Bailey, D. C. Eder, and S. L. Jacques, Appl. Opt. **36**(34), 9068 (1997).
[12] M. Friedman, M. Strauss, P. Amendt, R. A. London, and M. E. Glinsky, Phys. Fluids **14**(5), 1768 (2002).
[13] M. S. Plesset and R. B. Chapman, J. Fluid Mech. **47**(MAY31), 283 (1971).
[14] L. D. Landau and E. M. Lifshitz, *Fluid Mechanics* (Pergamon, New York, 1987), pp. 1–43, 251–312.
[15] A. Prosperetti and J. W. Jacobs, J. Comput. Phys. **51**(3), 365 (1983).
[16] J. R. Blake and D. C. Gibson, J. Fluid Mech. **111**(OCT), 123 (1981).
[17] M. Friedman and A. Kandel, in *Fuzzy Expert Systems*, edited by A. Kandel (CRC, Boca Raton, 1994).
[18] D. V. Palanker, M. F. Marmor, A. Branco, P. Huie, J. M. Miller, S. R. Sanislo, A. Vankov, and M. S. Blumenkranz, Arch. Ophthalmol. (Chicago) **120**(5), 636 (2002).
[19] A. Vogel, P. Schweiger, A. Frieser, M. N. Asiyo, and R. Birngruber, IEEE J. Quantum Electron. **26**(12), 2240 (1990).
[20] E. A. Brujan, K. Nahen, P. Schmidt, and A. Vogel, J. Fluid Mech. **433**, 251 (2001).
[21] I. Turovets, D. Palanker, Y. Kokotov, I. Hemo, and A. Lewis, J. Appl. Phys. **79**(5), 2689 (1996).
[22] L. Haar, J. S. Gallagher, and G. S. Kell, *NBS/NRC Steam Tables* (McGraw-Hill, New York, 1984).

Downloaded 12 Sep 2003 to 171.64.108.234. Redistribution subject to AIP license or copyright, see http://ojps.aip.org/japo/japcr.jsp